

Polymorphism, Nanostructures, and Barrier Properties of Ceramide-Based Lipid Films

Petra Pullmannová,* Barbora A. Čuříková-Kindlová, Veronika Ondřejčková, Andrej Kováčik, Kristýna Dvořáková, Lucia Dulanská, Robert Georgii, Adam Majcher, Jaroslav Maixner, Norbert Kučerka, Jarmila Zbytovská, and Kateřina Vávrová



Cite This: *ACS Omega* 2023, 8, 422–435



Read Online

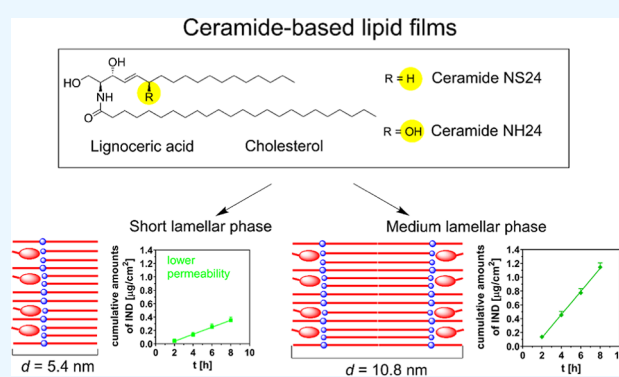
ACCESS |

Metrics & More

Article Recommendations

Supporting Information

ABSTRACT: Ceramides belong to sphingolipids, an important group of cellular and extracellular lipids. Their physiological functions range from cell signaling to participation in the formation of barriers against water evaporation. In the skin, they are essential for the permeability barrier, together with free fatty acids and cholesterol. We examined the periodical structure and permeability of lipid films composed of ceramides (Cer; namely, *N*-lignoceroyl 6-hydroxy-sphingosine, CerNH₂₄, and *N*-lignoceroyl sphingosine, CerNS₂₄), lignoceric acid (LIG; 24:0), and cholesterol (Chol). X-ray diffraction experiments showed that the CerNH₂₄-based samples form either a short lamellar phase (SLP, $d \sim 5.4$ nm) or a medium lamellar phase (MLP, $d = 10.63$ – 10.78 nm) depending on the annealing conditions. The proposed molecular arrangement of the MLP based on extended Cer molecules also agreed with the relative neutron scattering length density profiles obtained from the neutron diffraction data. The presence of MLP increased the lipid film permeability to the lipophilic model permeant (indomethacin) relative to the CerNS₂₄-based control samples and the samples that had the same lipid composition but formed an SLP. Thus, the arrangement of lipids in various nanostructures is responsive to external conditions during sample preparation. This polymorphic behavior directly affects the barrier properties, which could also be (patho)physiologically relevant.



INTRODUCTION

Whenever nature needs to create a barrier against desiccation or a waterproof coating, it employs hydrophobic compounds with long, saturated aliphatic chains and various functional groups. For example, leaves, stems, or fruits of most higher plants are protected from desiccation by cuticular and epicuticular waxes.¹ The cornea of the eye is coated with a tear film which contains various lipids to limit water evaporation from the corneal epithelium.^{2,3} The waxes waterproof the outermost part of the insect cuticles,⁴ and internal wool lipids impregnate sheep wool.⁵ Some of these water barrier solutions use long fatty acids, cholesterol (Chol), cholesterol-esters, and ceramides (Cer).^{5,6} The skin permeability barrier is not an exception. In the skin, mainly Cer, free fatty acids (FFAs), and Chol are involved in the formation of aligned multilamellar lipid stacks between corneocytes of the uppermost skin layer, the *stratum corneum* (SC).⁷ This highly organized lipid matrix acts as a barrier, which restricts water loss and hinders the entry of exogenous substances into the organism.⁸

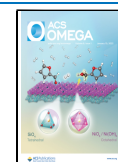
Ceramides with very long aliphatic chains are hydrophobic, solid at room temperature, melt without decomposing at the temperature of the main phase transition around 95 °C,^{9,10} and

have numerous thermotropic phase transitions.¹¹ Chemically, Cer are sphingolipids derived from a long-chain sphingoid base by attaching a fatty acid by an amide bond to an amino group in position 2.¹² Cer play a key role in cell signaling as the precursor of more complex sphingolipids and as the indispensable component of the skin permeability barrier.^{7,13,14} The best-explored area of sphingolipid biology is metabolism.^{15,16} Cer as a component of the cell membrane undergo lateral segregation and form ceramide-rich platforms.^{17,18} However, the molecular arrangement of extracellular skin lipids remains unclear.^{19–26} Electron microscopy has detected lamellar structures with a regular arrangement of broad/narrow/broad electron-lucent bands in SC lipids.²⁷ X-ray diffraction (XRD), which is sensitive to periodic fluctuations in electron density at the nanoscopic scale, revealed ~ 13 ,^{23,28,29} and ~ 6 nm³⁰ repeat distances in the SC along with an ~ 3.4 nm

Received: August 3, 2022

Accepted: December 2, 2022

Published: December 23, 2022



repeat distance coming from crystalline Chol.^{30,31} Ultralong Cer containing 30–34C acyl chains with linoleic acid ester-linked to ω -hydroxyl (ω -O-acylCer)³² were reported to be necessary for the formation of the lamellar phases with a long repeat distance.^{33,34} The molecular arrangement of skin lipid models was also investigated by neutron diffraction (ND).^{26,35–38}

It turned out that a structure with a rather long repeat distance of 10.6 nm can be formed in the Cer-based lipid models even without ω -O-acylCer—the medium lamellar phase (MLP).³⁹ The very first report on MLP was most likely published in 1993 by Parrott and Turner,⁴⁰ but this structure was for a long time considered to be nonrepresentative for SC.^{41,42} After several years, the very high magnification cryo-electron microscopy revealed the \sim 11 nm repeating unit of the SC lipid matrix in its near-native state.²⁵ MLP with $d \sim$ 10.6 nm, which is close to the reported 11 nm SC lipid unit, was detected in skin lipid models based on different Cer types: CerNS24 (*N*-lignoceroyl-*D*-erythro-sphingosine),³⁹ CerNH24 (*N*-lignoceroyl-*D*-erythro-6-hydroxysphingosine),⁴³ and the Cer analogue 3-deoxy-CerNS24.⁴⁴ A double-bilayer structure was proposed for MLP,⁴⁰ however, it has not been systematically investigated.

The aim of this study is to shed more light on the principles of the molecular organization of Cer-based multilamellar films. Such films serve as an approximation of aligned extracellular lipid stacks observed in SC. We studied the conditions of MLP formation in lipid models with various proportions of CerNH24 and CerNS24 (Figure 1) and its structure by

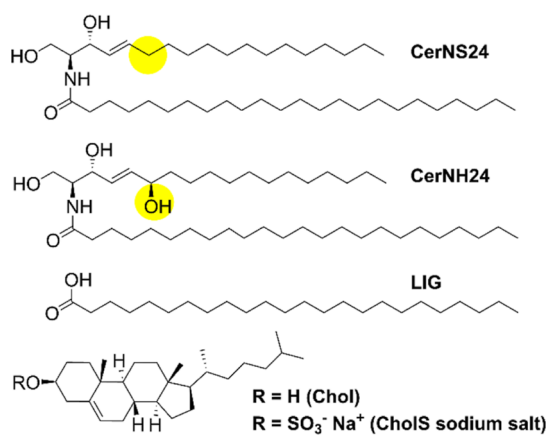


Figure 1. Chemical structures of the lipids (CerNS24, CerNH24, LIG, Chol, and CholS) used for the preparation of the lipid films.

XRD and ND. Moreover, we studied how the lipid films resist water loss and the selected permeants are permeated. CerNH24 is found exclusively in the skin and is therefore important for skin barrier function, although it is not the most abundant Cer species.⁴⁵ CerNH24 is structurally similar to CerNS24, and it only contains an additional hydroxy group in position 6 of the sphingoid backbone. Furthermore, CerNH24 is not commercially available, which limits the possibilities of its investigation.

EXPERIMENTAL SECTION

Chemicals and Materials. *N*-Lignoceroyl-*D*-erythro-sphingosine d18:1/24:0 (CerNS24) was purchased from Avanti Polar Lipids (Alabaster, AL, USA). *N*-Lignoceroyl-*D*-erythro-6-hydroxysphingosine d18:1/24:0 (CerNH24) was synthesized,

and its structure and purity were determined as described in ref 9. Cholesterol from lanolin (Chol), cholesteryl sulfate (CholS), tetracosanoic acid (LIG), theophylline (TH), indomethacin (IND), gentamicin sulfate from *Micromonospora purpurea*, sodium phosphate dibasic dodecahydrate, propylene glycol, and solvents were purchased from Sigma-Aldrich Chemie GmbH (Schnellendorf, Germany). Sodium hydroxide, sodium chloride, potassium chloride, sodium phosphate monobasic dihydrate, and potassium sulfate were supplied by Lachema (Neratovice, Czech Republic). The chemicals were of analytical grade and were used without further purification. All the solvents were of analytical or high-performance liquid chromatography (HPLC) grade. The aqueous solutions were prepared using ultra-pure water (Milli-Q RG water purification system, Millipore, Burlington, Massachusetts, USA). D₂O was provided by Heinz Maier-Leibnitz Zentrum (Garching, Germany). Nuclepore track-etched polycarbonate membranes with a 0.015 μ m pore size were from Whatman (Kent, Maidstone, United Kingdom). Esco 22 \times 22 mm² microscope cover glasses were from Erie Scientific LLC (Portsmouth, New Hampshire, USA). Borofloat 33 wafers 30 \times 60 \times 2 mm³ in size were from Schott Technical Glass Solutions, GmbH (Jena, Germany).

Preparation of Lipid Films for XRD and Permeation Experiments. The lipids (CerNH24, CerNS24, LIG, and Chol) were dissolved in 2:1 chloroform/methanol (v/v) and mixed at the molar ratios specified in Table 1. The molar ratio

Table 1. Compositions of the Lipid Films for the XRD and Permeation Experiments

| sample label | lipid film composition (molar ratios) | | | |
|--------------|---------------------------------------|---------|-----|------|
| | CerNH24 | CerNS24 | LIG | Chol |
| 0/100 | 0 | 100 | 100 | 100 |
| 12.5/87.5 | 12.5 | 87.5 | 100 | 100 |
| 25/75 | 25 | 75 | 100 | 100 |
| 37.5/62.5 | 37.5 | 62.5 | 100 | 100 |
| 50/50 | 50 | 50 | 100 | 100 |
| 62.5/37.5 | 62.5 | 37.5 | 100 | 100 |
| 75/25 | 75 | 25 | 100 | 100 |
| 87.5/12.5 | 87.5 | 12.5 | 100 | 100 |

of Cer/LIG/Chol = 1:1:1 was kept constant. The lipid mixtures were dried under a stream of nitrogen and in a vacuum and redissolved in 2:1 hexane/96% ethanol (v/v) at 4.5 mg/mL. Nuclepore polycarbonate filters were washed in 2:1 hexane/96% ethanol, and mounted in a steel holder with a 0.79 cm² circular opening. The lipid solutions (3 \times 100 μ L providing 1.35 mg lipids per 1 cm²) were sprayed on the polycarbonate filters under a stream of nitrogen at a flow rate of 10.2 μ L/min onto a 10 \times 10 mm² square using a Linomat V (Camag, Muttenz, Switzerland) equipped for additional y -axis movement.²² For XRD, the lipid solutions were sprayed onto cover glasses in the same manner. The lipid layer thickness was approximately 11 μ m.^{20,46}

The prepared lipid films were dried overnight in a vacuum and were stored at 2–6 $^{\circ}$ C. Before use, the lipid films were annealed by either of the following protocols (a,b).

- Annealing at 90 $^{\circ}$ C. The samples were placed on aluminum circular supports in empty aluminum containers and sealed. The containers with samples were heated

to 90 °C, equilibrated at this temperature for 10 min, and slowly (~3 h) cooled to room temperature.

- b) Annealing at 80 °C with H₂O. The samples were placed on aluminum circular supports upon a small amount of distilled water in aluminum containers and sealed (the water was not in contact with the lipids). In the case of the samples applied to glass supports, water vapor can penetrate through the film only from one side. To maintain consistent conditions for the films on cover glasses and polycarbonate filters, we placed a silicone rubber seal over one side of the opening of each steel holder. The margins of the silicone rubber seal were smeared with silicone grease to ensure its adhesion to the steel holder. The films applied to the polycarbonate filters were accessible to water vapor only from the lipidless side of the filter. The containers with samples were placed in an oven preheated to 80 °C, equilibrated at this temperature for 30 min, and slowly (~3 h) cooled to room temperature. This protocol was used to be consistent with the previous experiments.⁴³

XRD. The films were equilibrated at room temperature for at least 24 h before the XRD measurements. The XRD data were collected at room temperature, humidity, and atmospheric pressure with an X'Pert PRO θ - θ powder diffractometer (PANalytical B.V., Almelo, Netherlands) with parafocusing Bragg-Brentano geometry using Co K α radiation ($\lambda = 0.17903$ nm, $U = 35$ kV, $I = 40$ mA) in modified sample holders over the angular range of 0.6–30° (2θ). The data were scanned with an ultrafast position-sensitive linear one-dimensional (1D) X'Celerator detector with a step size of 0.0167° (2θ) and a counting time of 20.32 s step⁻¹.

The structure of the sample designed for ND was verified at room temperature and humidity using a D8 ADVANCE θ - θ (Bruker AXS GmbH, Karlsruhe, Germany) powder diffractometer with parafocusing Bragg-Brentano geometry using Co K α radiation ($\lambda = 0.17903$ nm, $U = 34$ kV, $I = 30$ mA). The data were scanned with an ultrafast detector, LynxEye, over the angular range 2–30° (2θ) with a step size of 0.0196° (2θ) and a counting time of 76.8 s step⁻¹.

The XRD data were evaluated using X'Pert Data Viewer software (PANalytical B.V., Almelo, Netherlands). The XRD patterns show the raw scattered intensity without normalization as a function of the magnitude of the scattering vector q [nm⁻¹], which is proportional to the scattering angle 2θ , according to the equation

$$q = \frac{4\pi \sin(\theta)}{\lambda} \quad (1)$$

where λ is the wavelength of the radiation. The diffractograms of the lamellar phases exhibit a set of Bragg reflections whose reciprocal spacings are in the characteristic ratios of

$$q_n = \frac{2\pi n}{d} \quad (2)$$

(diffraction index $n = 1, 2, 3, \dots$). The repeat distance d [nm] characterizes the spacing between adjacent scattering planes of parallel lipid layers arranged in a one-dimensional lattice in real space. The repeat distance d was obtained from the slope a of a linear regression of the dependence

$$q_n = a \cdot n + q_0 \quad (3)$$

where q_0 is a constant corresponding to a shift of the origin, according to the equation

$$d = \frac{2\pi}{a} \quad (4)$$

Selected samples were measured at room temperature and humidity with a D8 Discover microdiffraction system (Bruker AXS GmbH, Karlsruhe, Germany) using Co K α radiation ($\lambda = 0.17903$ nm, $U = 35$ kV, $I = 40$ mA). The sample was placed on the xyz programmable stage with x , y , and z translations in the range of 0–24 mm. The XRD was recorded at $\omega = 2.5^\circ$, which is the angle between the primary beam and the sample, and $\gamma = 10.5^\circ$, which is the angle between the Vantech two-dimensional (2D) detector and the sample. The beam irradiated the sample area of 14×0.3 mm² with a counting time of 3 min per image. The data were analyzed using the software package Bruker EVA 4.0 (Bruker AXS GmbH, Karlsruhe, Germany).

ND Experiments. The sample for the ND experiment was prepared from 15 mg of the CerNH₂₄/NS₂₄/LIG/Chol mixture at the molar ratio of 75/25/100/45 with 5 weight % of CholS. The lipids were dissolved in chloroform/methanol = 2:1 (v/v), and CholS was dissolved in methanol. The aliquots were mixed at the desired ratio, the solvent was evaporated, and the dry lipid mixture was redissolved in hexane/ethanol 96% = 2:1 (v/v) at the concentration of 4.5 mg/mL. The lipid solution was sprayed at the flow rate of 10.2 μ L/min on an 18×30 mm² area of a Borofloat 33 wafer using a Linomat V instrument (Camag, Muttenz, Switzerland) equipped for additional y -axis movement.²² The traces of the solvents were removed in a vacuum overnight, and the sample was annealed at 90 °C by protocol (a) described in the previous section. The thickness of the lipid layer was calculated to be 43 μ m.

The ND was measured using a cold-neutron three-axis spectrometer MIRA⁴⁷ located at the neutron source in Heinz Maier-Leibnitz Zentrum (Garching, Germany). The neutron radiation wavelengths $\lambda = 0.5026$ and 0.4490 nm were selected using the HOPG graphite monochromator and collimated using a 30" collimator. A HOPG graphite analyzer and a ³He detector were used. The beam dimensions were 5.00 \times 15.00 mm².

The sample was placed in the airtight humidity chamber and measured at three different contrast conditions (100, 63, and 8% D₂O in H₂O v/v) at 98% relative humidity (RH) achieved over the saturated K₂SO₄ solution at $T = 32$ °C. Before measurement, the sample was equilibrated at the given contrast conditions for 1 h. Before the θ - 2θ -scan, the rocking curve of the sample was recorded by rotating the sample position with the detector fixed at a Bragg position, corresponding to the 2nd order reflection ($2\theta = 5^\circ$, $\lambda = 0.4490$ nm). The precise position of the sample in the beam was set using a goniometer according to the rocking curve, which yielded the highest intensity of the reflections. A θ - 2θ -scan (θ = sample angle; 2θ = detector angle, $\lambda = 0.5026$ nm, step size $2\theta = 0.075^\circ$) with the detector rotating double the sample angle was performed to obtain diffraction patterns as a function of the scattering vector q . The acquisition time for a single sample at one contrast condition was ~8–10 h. The detected intensity was converted to one-dimensional diffraction patterns as a function of the scattering angle 2θ and normalized to the incoming flux and acquisition time. The 2θ angle was converted to the scattering vector q according to eq 1. The ND reflections were

fitted by the Gaussian–Lorentzian Cross-Product function above the linear background using OriginPro 2018b software. The 1st order reflections were fitted by the same function above the background fitted by the two-phase exponential decay function using the same software. The fitted peak parameters served for further calculation. The intensities I_h (fitted peak areas) were corrected for the incident flux (C_{flux}), the sample absorption (C_{abs}), and the Lorentz factor (C_{Lor}), as was described⁴⁸ using the following equations

$$C_{\text{flux}} = \frac{1}{\text{erf}\left(\frac{L \sin(\theta)}{\sqrt{8} \sigma}\right)} \quad (5)$$

where erf is the error function, L is the sample length (~ 2 cm), and 2σ is the beam width (0.5 cm).

$$C_{\text{abs}} = \frac{\frac{2\mu t}{\sin(\theta)}}{1 - \exp^{-2\mu t/\sin(\theta)}} \quad (6)$$

where t is the sample thickness (~ 0.0043 cm), and μ ($\sim 5.6\text{--}6$ cm⁻¹) is the absorption coefficient. The sample thickness t was estimated from the applied amount of lipid, sample area, and assumptive dry lipid density ($\rho \sim 0.87$ g cm⁻³) reported in ref 37. The absorption coefficient μ was calculated from the total neutron cross-section (i.e., the sum of the coherent and incoherent scattering cross-sections and the absorption cross-section) of all the elements at the used wavelength (data from the NIST Center for Neutron Research), density, and the chemical composition of the sample according to the equation

$$\mu = \frac{\sum N_i \varphi_i}{V} \quad (7)$$

where N_i is the number of specific atoms i , φ_i is the total neutron cross-section, and V is the volume of the sample. The hydration of the sample at various contrast conditions was included in the μ calculation, so we added two water molecules per lipid.³⁷ The Lorentz correction was calculated as

$$C_{\text{Lor}} = \sin(2\theta) \quad (8)$$

The Lorentz correction in eq 8 applies for the well-aligned (oriented) lamellae and can be different for samples with more mosaic spread.^{49,50} The absolute values of scattering form factors for various orders h were calculated using the equation

$$|F_h| = \sqrt{C_{\text{flux}} C_{\text{abs}} C_{\text{Lor}} I_h} \quad (9)$$

where I_h is the scattering intensity of the individual order. The phase angles were assessed according to the H₂O–D₂O exchange method described in ref 51 and will be discussed in Results. The relative neutron scattering length density (NSLD, $\rho_{(z)}$) profiles across the lipid layer with the origin ($z = 0$ nm) in its middle were calculated according to the equation

$$\rho_{(z)} = \sum_{h=1}^{h_{\text{max}}} F_h \cos\left(\frac{2\pi h z}{d}\right) \quad (10)$$

The form factor errors δF_h were derived from the uncertainties of experimental intensities expressed as the square root of the integrated intensity I_h of each reflection and included in the calculations of the uncertainties of the reconstructed NSLD profiles. Note that the approach of NSLD error estimation is not unified in the literature.^{26,37,38,51–57} The

uncertainties of the relative NSLD profile ($\delta\rho_{(z)}$) were calculated according to ref 58 from the following equation

$$\delta\rho_{(z)} = \pm \left[\sum_{h=1}^{h_{\text{max}}} (\delta F_h)^2 \cos^2\left(\frac{2\pi h z}{d}\right) \right]^{1/2} \quad (11)$$

The theoretical continuous form factor was calculated via the equation inverse to eq 10

$$F_{(q)} = \int_0^\infty \rho_{(z)} \cos(qz) dz \quad (12)$$

that is true for centrosymmetric systems implied in this study.⁵⁹

Permeation Experiments. The permeability of the model lipid films was evaluated using Franz diffusion cells with an available diffusion area of 0.5 cm² and an acceptor compartment of approximately 6.5 mL. The precise volume for each cell was measured individually and was included in the calculation. The annealed samples were equilibrated at 32 °C for 24 h and were then removed from the steel holders and mounted in Teflon holders. The samples were fixed between the upper and lower parts of the Franz cells, with the lipid film facing the donor compartment. The margins of the holders and diffusion cells were smeared with silicone grease to ensure their mutual adhesion. The acceptor compartment of the cell was filled with phosphate-buffered saline (PBS) solution, pH 7.4, containing 50 mg/L gentamicin and stirred at 32 °C. The samples were left to equilibrate for 68 h.

After equilibration, water loss (see below) was measured. The next day, 100 μ L of the first donor sample, a 5% theophylline (TH) suspension in 60% propylene glycol in water, was applied to the samples. Samples of the acceptor phase (300 μ L) were collected every 2 h over an 8 h period and were replaced by the same volume of PBS. During this period, a steady-state situation was reached. After the first 8 h of the permeation experiment, the applied donor suspension was carefully washed with PBS at pH 7.4, and the residual PBS was removed using cellulose swabs. The acceptor phase was removed and replaced with fresh PBS at pH 7.4. The samples were equilibrated for 12 h. Then, 100 μ L of a 2% indomethacin (IND) suspension in 60% propylene glycol in water was applied. The permeation experiment was repeated as described above. By conducting the experiment with IND on fresh samples, we previously verified that the first permeation experiment with TH did not alter the outcome of the second experiment with IND.^{60,61} The TH- and IND-containing samples were measured using isocratic reverse-phase HPLC. For further details on the data evaluation and statistics, see the Supporting Information. The data are reported as the steady-state flux of theophylline (TH) [μ g/cm²/h] and indomethacin (IND) [μ g/cm²/h], henceforth referred to as the flux of TH and IND. For further validation and comments, see our previous work.⁴⁶

Measurement of Water Loss through Lipid Films. The water loss through model films was measured using equipment for transepidermal water loss measurement, namely, an Aquaflux AF200 (Biox Systems Ltd, London, England) with a condenser-chamber with sensors for RH and temperature. The Franz cell was removed from the water bath; its upper part was removed, and the probe was placed on the Teflon sample holder with a 0.5 cm² circular opening. The average steady-state value was recorded using Aquaflux Software Version 9.3. Each sample was measured twice in the interval of

approximately 3 h, and an average of these two values was used. We did not place the measurement chamber directly on the lipid film but tightly on the surface of the Teflon holder with a circular opening. Thus, the measurement chamber adsorbed the water vapor from a larger area (0.5 cm²) exposed by Teflon holders than the area of the chamber hole itself (0.385 cm²). The obtained raw water loss values are therefore presented in arbitrary units.

RESULTS

The periodic structure of the CerNH24/CerNS24/LIG/Chol films prepared at various Cer molar ratios (Table 1) was detected by XRD. The 1D XRD patterns (Figures 2 and 3)

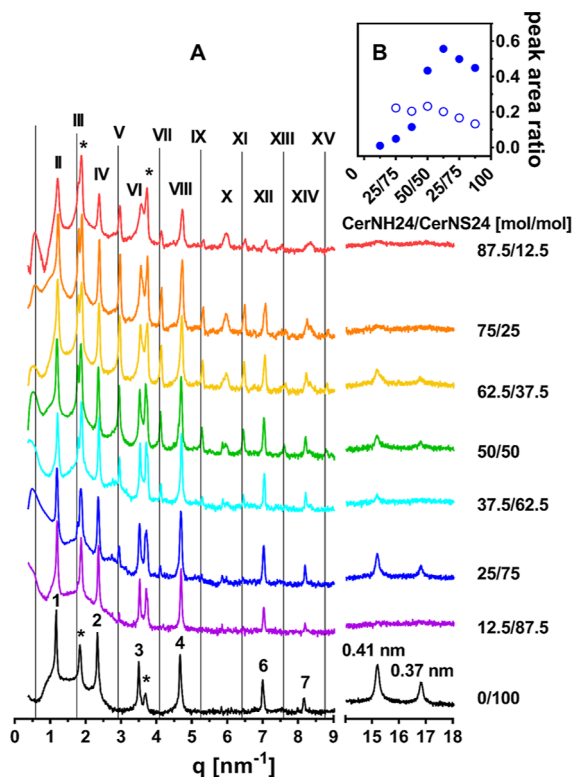


Figure 2. XRD patterns of the CerNH24/CerNS24/LIG/Chol samples prepared at the 0/100/100/100–87.5/12.5/100/100 molar ratios annealed at 90 °C (panel A). Arabic numerals indicate the SLP reflections; Roman numerals indicate the MLP reflections; asterisks indicate the separated Chol reflections. Grid lines predict the position of odd MLP reflections. The relative intensities are shown on a logarithmic scale. The area of the XRD peak at $q \sim 2.95 \text{ nm}^{-1}$ (5th order of the MLP) in the ratio to the area of the XRD peak at $q \sim 2.35 \text{ nm}^{-1}$ (attributable to the 2nd order of the SLP and the 4th order of the MLP) as a function of the CerNH24/CerNS24 molar ratio in the samples annealed at 90 °C (panel B, filled circles). The area of the XRD peak at $q \sim 4.1 \text{ nm}^{-1}$ (7th order of the MLP) in the ratio to the area of the XRD peak at $q \sim 2.95 \text{ nm}^{-1}$ (5th order of the MLP) as a function of the CerNH24/CerNS24 molar ratio in the samples annealed at 90 °C (panel B, open circles).

show the raw XRD intensity on the logarithmic scale as a function of the scattering vector q (nm⁻¹). The small-angle XRD region (SAX) of patterns contains information about the periodic structure in the direction perpendicular to the lamellar plane, and the wide-angle XRD region (WAX) is related to the regular in-plane arrangement of lipid chains. The list of all

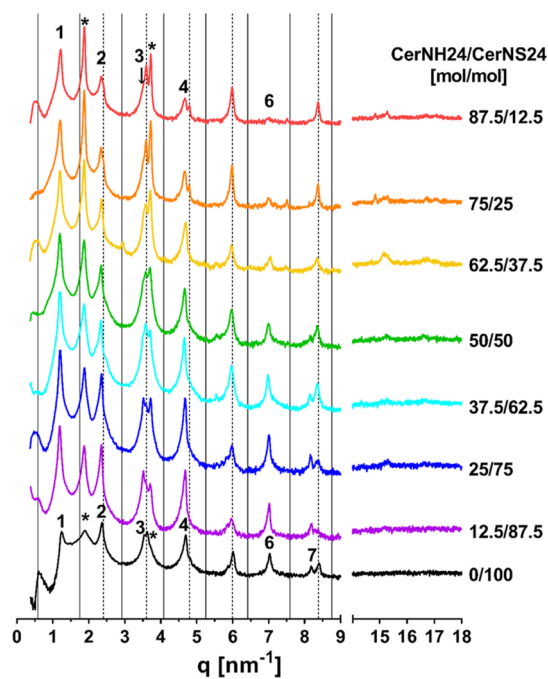


Figure 3. XRD patterns of the CerNH24/CerNS24/LIG/Chol samples prepared at the 0/100/100/100–87.5/12.5/100/100 molar ratios annealed at 80 °C/H₂O. Arabic numerals indicate SLP reflections; asterisks indicate separated Chol reflections; full grid lines predict the position of odd MLP reflections; dashed grid lines mark the positions of the separated LIG peaks. The relative intensities are shown on a logarithmic scale.

detected XRD reflections is in Tables S1 and S2, Supporting Information.

SAX Measurements. Lipid Films Annealed at 90 °C. The CerNS24/LIG/Chol sample, that is, without CerNH24 (hereafter referred to as the 0/100 sample), served as a control. The 0/100 sample had several regularly spaced reflections in SAX (black line in Figure 2A), which were attributed to the diffraction orders 1, 2, 3, 4, 6, up to 9 (only the 1st to the 7th order reflections are shown here for clarity) of the parallel lipid lamellae, providing a repeat distance $d = 5.40 \text{ nm}$. This lamellar stacking corresponded to the short lamellar phase (SLP), frequently reported for many skin barrier models.^{32,46,62} Furthermore, reflections of separated Chol were found (at $q = 1.84, 3.68 \text{ nm}^{-1}$), which are also typical for skin barrier models^{41,46} and the SC.³⁰

The sample with the lowest fraction of CerNH24, that is, the 12.5/87.5 sample (violet line, Figure 2A), formed an SLP phase of $d = 5.40 \text{ nm}$ and separated Chol. We also found weak additional peaks at $q \sim 1.78 \text{ nm}^{-1}$ (a shoulder of the Chol reflection at $q = 1.87 \text{ nm}^{-1}$) and $q = 2.94 \text{ nm}^{-1}$. These additional reflections were more pronounced in the samples with even higher fractions of CerNH24 and lower contents of CerNS24. In the 25/75 sample, reflections at 1.76, 2.93, and 4.09 nm⁻¹ were detected, along with the strong reflections attributable to SLP.

Additional reflections were found in the range of CerNH24/CerNS24 molar ratios of 25/75–87.5/12.5 and were assigned to the odd orders of the MLP, resulting in $d = 10.78\text{--}10.63 \text{ nm}$. The strong reflections attributable to the SLP could also be assigned to the MLP as the reflections of even orders 2, 4, 6, ... up to 18,³⁹ as the MLP is twice as long as the SLP. The SLP and MLP represent commensurate phases;^{39,63} thus, these



Figure 4. The 2D XRD patterns of the selected CerNH₂₄/CerNS₂₄/LIG/Chol samples with the indicated CerNH₂₄/CerNS₂₄ ratio. The filled arrows indicate the primary beam residue, and the empty arrows indicate the diffraction intensity in the WAX region.

samples contained either an MLP or an MLP coexisting with an SLP. The sample containing CerNH₂₄ as the only Cer mixed with FFA (16:0–24:0), Chol, and CholS formed an MLP with $d = 10.6$ nm and has been described elsewhere.⁴⁵

Some of the XRD patterns of the samples annealed at 90 °C also contained weak additional reflections at $q = 2.76, 5.95,$ and $11.10–11.14$ nm⁻¹. These reflections were not unambiguously attributable to the phases identified in the samples. A weak peak or elevated background occurred at very low q values <1 nm⁻¹, but it was poorly resolved and could have been a residue of scattering. Because of this uncertainty, such reflections were not attributed to any phase.

It is difficult to distinguish the MLP and SLP/MLP coexistence in the abovementioned sample series. The XRD patterns of the MLP were typical with more intense even orders and less intense odd orders. Similar XRD patterns were described for nerve myelin,⁶⁴ L γ phases (described in phospholipids,⁶⁵ phospholipid–peptide complexes,⁶⁶ and pulmonary surfactant⁶⁷), and oriented fatty acid bilayers with well-defined asymmetric distribution of lipids.⁶³ Therefore, the low intensity of odd orders alone does not indicate a low proportion of MLP in the sample. We estimated the areas of the peak at $q \sim 2.95$ nm⁻¹ (indicative of the 5th order of the MLP) and of the peak at $q \sim 2.35$ nm⁻¹ [attributable to either the SLP (2nd order) or the MLP (4th order)]. The variation in the area ratios ($A_{2.95}/A_{2.35}$) approximately estimated the changes in the SLP and MLP proportions in the samples (Figure 2B). The $A_{2.95}/A_{2.35}$ ratios were low in the samples with low CerNH₂₄ contents, sharply increased in the 50/50 sample, and remained approximately constant with a further increase in the CerNH₂₄ contents. We estimated that the SLP and MLP most likely coexisted in the samples with CerNH₂₄/CerNS₂₄ $< 50/50$. The area of the 7th order of MLP ($q \sim 4.1$ nm⁻¹) in a ratio to the area of the 5th order ($q \sim 2.95$ nm⁻¹) did not undergo such a remarkable change relative to the $A_{2.95}/A_{2.35}$ (Figure 2B).

Lipid Films Annealed at 80 °C with H₂O. All the studied samples were also annealed at 80 °C/H₂O to mimic the sample preparation used previously.⁴³ Variation in the annealing conditions could reveal the putative lipid polymorphism. Indeed, these lipid films, with one exception, formed an SLP with $d = 5.45–5.37$ nm (Figure 3). The exception was the 62.5/37.5 sample, which also showed a weak reflection at $q = 2.95$ nm⁻¹, which was indicative of an MLP. There were also some differences in the relative intensity of the XRD patterns of individual samples, which can be of multiple origins. Separated Chol and an additional phase coexisted with the lamellar phase in the lipid films. The additional reflections or shoulders were found at $q \sim 2.41, 3.60, 4.80, 5.99, 8.38,$ and

10.77 nm⁻¹ (not all the peaks/shoulders were found in all the patterns). These peaks were attributed to a separated crystalline LIG and assigned the diffraction indices (hkl) = (002), (003), (004), (005), (007), and (009), respectively. According to the crystallographic data of long-chain carboxylic acids, the C-form of crystalline LIG forms a monoclinic lattice, and we have interpolated its cell dimensions according to⁶⁸ [$a = 0.93$ nm, $b = 0.50$ nm, $c = 6.60$ nm, $\beta = 127.39^\circ$ and $d(001) = 5.25$ nm]. A similar LIG-rich phase with $d \sim 5.2$ nm was previously observed in other model lipid films.⁴⁶

WAX Measurements. Lipid Films Annealed at 90 °C. The 0/100 sample showed two strong reflections in WAX (black line in Figure 2A) corresponding to the repeat distances of the diffracting planes ~ 0.41 and ~ 0.37 nm. These reflections were attributed to the orthorhombic lateral packing of polymethylene chains.²² The peak positions allowed the calculation of the area per lipid chain A_{ch} in the plane perpendicular to the chain axis according to ref 69 providing a value of 0.186 nm². The value was consistent with that previously published for orthorhombic lateral chain packing in the CerNS-based model⁶¹ and the crystalline Cer analogue *N*-(2D,3D-dihydroxyoctadecanoyl)-phytosphingosine.⁷⁰ A similar A_{ch} was obtained for the triclinic lateral chain packing of crystalline *N*-tetracosanoylphytosphingosine (0.188 nm²; ref 71 cited in ref 69). The lipid chains in the 0/100 model were packed very tightly, comparable to crystalline Cer. Such a tight arrangement is not possible with incorporated Chol molecules, which have a disordering effect on the rigid lipid chains.⁷² The orthorhombic packing thus comes from the Chol-free domains.

The WAX of the CerNH₂₄-containing samples (Figure 2A) comprised either no or weak reflections corresponding to the lateral lipid chain packing and contrasted with the WAX of the 0/100 sample. The detection of the peaks in the WAX region depends on the degree of sample alignment. If the samples are well aligned, the WAX peaks of the aligned lamellae cannot be detected with the 1D detector in the meridional direction, where the reflections of the long-range arrangement occurred. Because the samples attained various degrees of alignment, we detected either strong or weak reflections of the orthorhombic arrangement or none at all.

To confirm the effect of alignment on the WAX reflection intensities, additional XRD measurements of the selected samples (0/100, 25/75, and 50/50) were performed on a diffractometer equipped with a 2D detector (Figure 4). The 2D detector covered a larger part of the reciprocal space and collected Debye–Scherrer rings. The diffraction intensity in the 2D image of the 0/100 sample (Figure 4) was mostly distributed in the Debye–Scherrer rings, and a smaller part seemed to be concentrated in the tiny spots apparent in the

meridional direction in the SAX region. This observation indicated a prevalent polycrystalline character of 0/100, in which most of the lipid domains do not attain the preferred orientation relative to the plane of a supporting wafer. The WAX region showed strong Debye–Scherrer rings with clearly resolved reflections of orthorhombic chain packing of randomly oriented lipid domains.

In contrast, the 2D XRD patterns of the 25/75 and 50/50 samples showed the diffraction intensity of the SAX reflections mostly concentrated in the spots located in the meridional direction. This indicated that the planes of the lipid lamellae were mostly aligned parallel to the plane of the supporting wafer.^{73,74}

The WAX reflections of the 25/75 and 50/50 samples were weak and unevenly distributed along the Debye–Scherrer rings. The orthorhombic sublattice, which provides reflections detectable in the WAX region, is a structure perpendicular or nearly perpendicular to the plane of the lipid lamellae. Therefore, orthorhombic reflections must be located in the direction perpendicular or nearly perpendicular to the meridional direction of the SAX reflections, that is, in the equatorial direction.^{75–77} This part of the reciprocal space (the equatorial direction) is covered neither by the 2D nor by the 1D detector. The weak intensity in the WAX region distributed along the Debye–Scherrer rings originated from a small fraction of lipid lamellae with a random orientation. The high degree of lipid alignment caused the vanishing WAX reflections. Similar effects were reported in the study of plant epicuticular waxes.⁷⁸

Lipid Films Annealed at 80 °C with H₂O. There were mostly no reflections in the WAX region of the samples annealed at 80 °C/H₂O (Figure 3). Some weak reflections were found in 62.5/37.5 ($q = 14.85 \text{ nm}^{-1}$ corresponding to $\sim 0.42 \text{ nm}$), 75/25 ($q = 15.16 \text{ nm}^{-1}$ corresponding to $\sim 0.41 \text{ nm}$), and 87.5/12.5 ($q = 14.84$ and 15.28 nm^{-1}). A reflection corresponding to $\sim 0.42 \text{ nm}$ was previously described in a Cer/palmitic acid/Chol mixture and was attributed to a hexagonal arrangement of lipid chains.⁷⁹ However, it is not clear whether these reflections belong to the lipid chain arrangement or some of the separated compounds (Chol, LIG). The missing reflections of the tight lipid chain packing were linked to the alignment of the lipid lamellae annealed at 80 °C/H₂O. For additional data and comments, see Figure S1, Supporting Information.

ND Experiment. An MLP-forming sample, the CerNH24/CerNS24/LIG/Chol/CholS mixture at the molar ratio 75/25/100/45/13, was studied by ND. The Chol content was decreased relative to the samples studied above to suppress its phase separation and possible convolution of Chol reflection with the 3rd order lamellar reflection. Furthermore, 5 weight % CholS, which represents one of the minor polar components of SC lipids, was added to the sample to increase its hydration ability. Hydration of the sample is needed to achieve the isomorphous hydrogen–deuterium replacement of exchangeable hydrogen atoms (including those on water molecules).⁸⁰ The structure of the sample was evaluated prior to the ND experiment by XRD in the q range of ~ 1.2 – 18 nm^{-1} , and the $d = 10.82 \text{ nm}$ was determined using the reflections from the 3rd up to the 20th order (Figure S2, Supporting Information).

ND was measured under three different contrast conditions (100, 63, and 8% D₂O v/v) at 98% RH achieved over the saturated K₂SO₄ solution at $T = 32 \text{ °C}$ (Figure 5A). The rocking curve of the sample (Figure 5B) provided a sharp peak

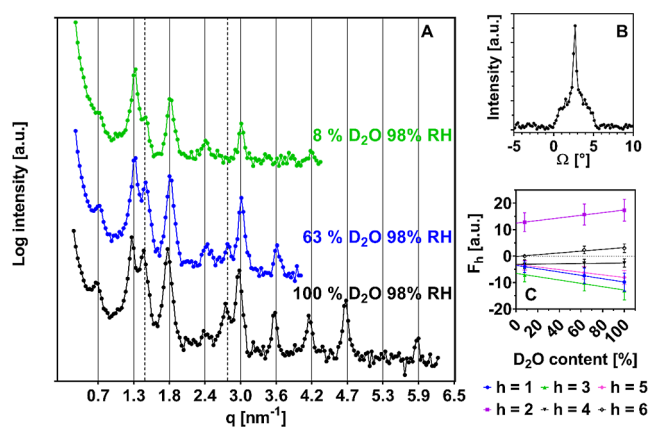


Figure 5. ND patterns measured under the indicated contrast conditions and 98% RH (panel A). The full grid lines predict the position of the MLP reflections ($d = 10.81 \text{ nm}$), and the dashed grid lines mark additional peaks. Rocking curve: diffraction intensity of the sample measured as a function of sample rotation (Ω angle) at the fixed detector position (2θ angle = 5° , $\lambda = 0.4490 \text{ nm}$) (panel B). The form factors F_h were evaluated according to⁵¹ as a function of the D₂O content (panel C).

superimposed over a broad peak. The sharp peak was fitted with a Lorentzian function⁵⁰ over a broad background approximated with a polynomial function using OriginPro 2018b software, yielding the full width at half maximum (FWHM) = 0.281° . The broad peak was fitted with a Gaussian function providing the FWHM value of 3.344° , which nevertheless corresponds to less than 1% misorientation (i.e., randomly oriented multilayers such as multilamellar vesicles would scatter into 360°). The FWHM value refers to the degree of lipid lamella alignment. The lower the value, the better the alignment and quality of the sample. For example, FWHM = 0.275° of the SC model was reported in ref 37, but it can be much lower for phospholipid-based bilayers (FWHM = 0.03° in ref 48). The two overlapped peaks in the rocking curve most likely represented two populations of lipid microcrystalline domains, each of them with a different mosaic spread. Since the effective Lorentz factor also depends upon the lamellar orientation, it should be corrected for this; otherwise, the F_h factors at higher q can be underestimated. As will be shown later, the experiment aimed to reveal the very basic structuring of MLP, so we did not accede to the correction of the Lorentz factor for the mosaic spread. The used Lorentz factor was calculated according to eq 8 for oriented samples.

The ND patterns (Figure 5A) showed a sequence of equidistantly spaced reflections. The repeat distance was calculated according to eqs 3 and 4 from nine reflection orders of the pattern at 100% D₂O, yielding $d = 10.80 \text{ nm}$. The obtained d -value agreed well with that determined by XRD (Figure S2, Supporting Information; $d = 10.82 \text{ nm}$). The q range measured at 100% D₂O was wider relative to that at 63 and 8% D₂O and provided a better estimate of the background. In addition to the expected peaks of lipid lamellae, we detected additional reflections that provided the distances of diffracting planes 4.39 and 2.26 nm, which can be the 1st and 2nd orders of an unknown phase. The preliminary XRD was measured in the q -range allowing the detection of the 2nd order of this phase, but no such indication has been found. The Chol peaks

were not apparent in the ND patterns due to the decreased Chol content.

The ND reflections were fitted with OriginPro 2018b software, and the fitted peak areas were used to calculate the absolute values of the form factors ($|F_h|$). In the first attempt, the phase angles of the form factors were determined according to the method described by Franks and Lieb.⁵¹ The form factors of a centrosymmetric unit cell change linearly with the isotopic composition of water vapor, and phase angles attain the values of either 1 or -1 (henceforward denoted as + or $-$). In this model, the origin ($z = 0$) is set in the center of the lipid layer, and the water distribution peaks are assumed to be Gaussian functions located at the positions $d/2$ from the center. Under these conditions, when H_2O is replaced by D_2O , the even-order form factors will increase algebraically, and the odd-order form factors will decrease algebraically. The linear plots of the form factors, depending on the D_2O content, should have positive slopes for even orders and negative slopes for odd orders.⁵¹ The phases were assigned according to this rule, and we yielded a combination of phases $- + - + - +$ (Figure 5C). All the calculated correction factors and $|F_h|$ are summarized in Table S3, Supporting Information.

The NSLD profiles calculated in arbitrary units under various contrast conditions are shown in Figure 6. Calculating

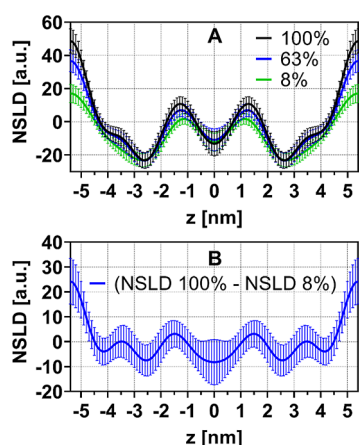


Figure 6. NSLD profiles of the sample reconstructed from six F_h factors (panel A). The profiles were shifted on the y-axis for better clarity. The error bars indicate the uncertainty of the NSLD profiles. The differential profile (100% D_2O –8% D_2O) is related to the water distribution across the lamella (panel B).

the NSLD profiles in absolute units requires the inclusion of the forward scattering factor (related to the offset of the NSLD profile) and the absolute scaling factor,⁴⁸ which we cannot calculate because of the lack of additional data.⁸¹ Therefore, the NSLD profiles in Figure 6A are presented on a relative scale. Generally, the lowest NSLD in the lipid layer profiles corresponds to terminal CH_3 groups of hydrophobic chains arranged without interdigitation.⁵¹ The NSLD of 8% D_2O is equal to ~ 0 ; therefore, the difference between the NSLD profiles at 100% D_2O and 8% D_2O is related to the water distribution profile (Figure 6B). Maximum hydration of SC lipid models was reported to be ~ 2 water molecules per one lipid molecule,³⁷ which is a very low level relative to phospholipid-based membranes. All the molecules of lipid films (Cer, FFA, and Chol) contain exchangeable hydrogen atoms. The long-term kinetics of the 1H – 2H exchange is unknown, although the effects of temperature on these

processes have been reported in pure Cer^{82,83} and SC models.⁸⁴

Moreover, the involvement of functional groups with exchangeable hydrogens (hydroxyl, amide, and carboxyl) in H-bonding can affect their availability for 1H – 2H exchange.⁸⁵ Therefore, the changes of NSLD at various contrasts were also related to 1H – 2H exchange in the functional groups of lipid molecules.

There are two maxima at $z = \pm d/2$ nm in the NSLD profiles (Figure 6A). The NSLD is also elevated in the middle of the profile (local maxima at $z \sim \pm 1.3$ nm), forming a central band with a width (distance between maxima) of ~ 2.6 nm. This profile resembled that published for SC models with $d = 12.9$ nm, reconstructed from nine diffraction orders.³⁸ All contained a central band of the elevated NSLD, which was broader relative to our profile (4.2 vs 2.6 nm). The side bands in our profiles (from $z = \pm 1.3$ nm to $z = \pm 5.4$) are 4.1 nm wide. Together with a 2.6 nm domain, they formed a sequence of three bands.

Both CerNH24 and CerNS24 contain a C24 acyl chain (approximate length in all-trans conformation is 3 nm) and a C18 sphingosine chain (approximately 2 nm in all-trans conformation). The length of LIG is similar to that of the Cer acyl chain (~ 3 nm). Thus, the central 2.6 nm domain in the obtained NSLD profiles seems to be too narrow to accommodate a bilayer in the proposed double-bilayer model⁴⁰ formed from these lipids. The profiles appear more likely to correspond to a triple bilayer (broad/narrow/broad sequence) rather than a double-bilayer. Franks and Lieb⁵¹ developed the method for a centrosymmetric system of phospholipid bilayers separated by water layers and arranged in a lamellar structure. The SC lipid assembly does not fit very well with this model since it forms a continuous lipid matrix (i.e., without the separate water layer) as was shown by electron microscopy and other methods independent of the interpretation of diffraction experiments.^{25,27,86,87} Therefore, we attempted to overcome the bias linked to the preexisting model and only assumed a central symmetry in our system. Note that this means breaking the rule of alternating slope signs as considered above.⁴⁸

We created the NSLD profiles from the first five orders (1st, 2nd, 3rd, 4th, and 5th) using all possible combinations of phase angles (signs) for a centrosymmetric system (Figure S3, Supporting Information). Couples of profiles shifted on the z scale by $d/2$ were marked by the letters A–P, meaning that these couples have the same NSLD distribution, but the origin of the z scale is either in the middle of the lipid layer or in the middle of the hydrophilic part. The criterion for plausibility was a predominance of domains with relatively low NSLD, as most of the used molecules contain long polymethylene chains with strong hydrophobic interactions. Only few of the phase angle combinations provided plausible NSLD profiles. The profiles A and B in Figure S3, Supporting Information, can be considered plausible, whereas profile C corresponds to that obtained using Franks and Lieb's method and was discussed above. Profile D showed the NSLD distribution similar to that in C. Profiles A and B comprise a broad domain with a width of ~ 6.8 and ~ 6.6 nm, respectively (calculated as the distance between local NSLD maxima). Moreover, these profiles showed only two peaks of relatively high NSLD and thus formed only two alternating domains of lower NSLD (~ 6.8 and ~ 4.1 nm wide).

The plausible NSLD profiles with the center of the symmetry in the middle of the hydrophobic domain were further refined by the addition of the remaining four F_h factors. All the possible combinations of phase angles related to the added F_h factors were calculated. The combinations providing the most plausible results are depicted in Figure 7, panels A

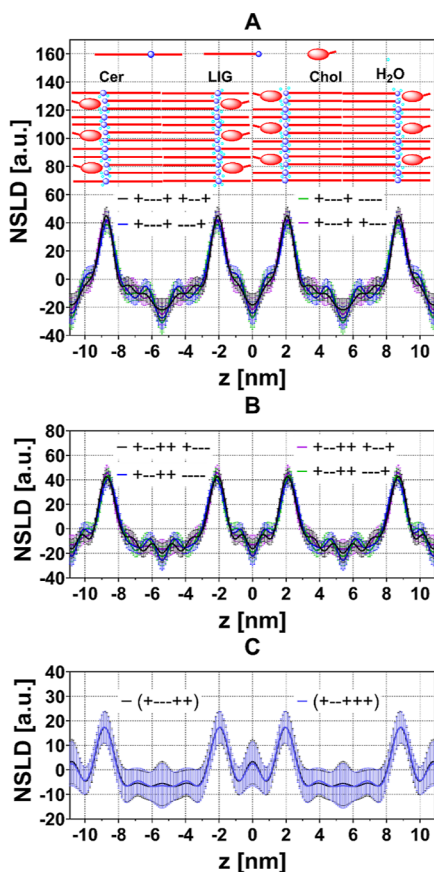


Figure 7. NSLD profiles of the sample reconstructed from nine F_h factors at 100% D₂O (panel A, B) at the indicated phase angle combinations. The putative arrangement of the major lipid classes is depicted in panel A. The position at $z = 0$ nm is the center of the lipid lamella. The differential profiles (100% D₂O–8% D₂O) for the selected phase angle combinations related to the water distribution are shown in panel C.

and B. These combinations of phase angles were further used to calculate the NSLD profile of the sample at 8% D₂O, as the F_h did not change their phases in dependence on the contrast conditions. The difference between the profiles at 100 and 8% D₂O was related to the D₂O distribution across the lamella. The phase angle combinations providing plausible D₂O distribution are shown in Figure 7C. The relative NSLD of the hydrophobic domains in D₂O distribution profile is, similarly to Figure 6B, slightly negative. We speculate further in the discussion about possible reasons.

The selection of phase angles was corroborated by the calculations of continuous form factors of the selected relative NSLD profiles according to eq 12. The continuous Fourier transforms were compared with the discrete form factors obtained from the experimental diffraction intensities (Figure 8). The comparison does not show any obvious shortfalls that would suggest the exclusion of some of the discussed profiles, while confirming their plausibility.

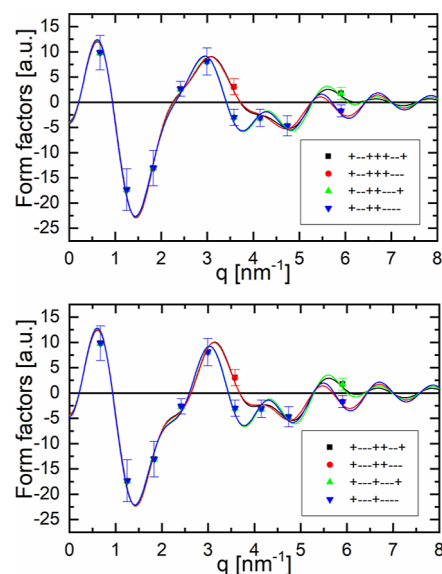


Figure 8. Continuous form factor calculated as a Fourier transform of the relative NSLD profiles reconstructed from the F_h factors with indicated phase angles (signs).

The putative molecular arrangement of these phases in Figure 7 is based on the extended conformation of Cer molecules, where each domain corresponds to approximately double the length of the lipid polymethylene chains. Here, the Cer acyl chain prefers the interaction with LIG. Such a domain could be a source of the orthorhombic polymethylene chain packing. The sphingosine acyl chain preferentially interacts with Chol. This arrangement of SC lipids was previously suggested based on electron microscopy,^{25,87–89} Fourier transform infrared spectroscopy,⁹⁰ solid-state nuclear magnetic resonance,⁹¹ and XRD.³⁹ The model proposed here does not address the location of CholS and is not supposed to reveal structural details, but it suggests a plausible lipid organization within the MLP that would fit the narrow and wide domains in the NSLD profiles.

Permeation Experiment. Next, the effects of the lipid periodical structure on the barrier properties were studied. We selected the 0/100 (control), 25/75, and 50/50 samples, all of which were annealed at either 90 or 80 °C/H₂O and formed an SLP and/or an MLP. Three markers were used to assess the permeability of the selected models (Figures 9 and S4, Supporting Information): the water loss [a.u.], the flux of TH, and the flux of IND. TH and IND were selected due to their different physicochemical properties: TH is a small molecule with balanced lipophilicity ($M = 180.2$ g/mol, $\log P \sim 0$), whereas IND ($M = 357.8$ g/mol, $\log P \sim 4.3$) is larger and more hydrophobic than TH.

The water loss of the samples varied from 5.1 ± 0.5 a.u. (in 0/100 samples annealed at 90 °C) to 8.0 ± 1.3 a.u. (in 50/50 samples annealed at 80 °C/H₂O). The apparent changes in water loss among the studied samples were not statistically significant at $p < 0.05$.

The TH flux was not significantly affected by the CerNH24 content or the annealing method, although a trend toward decreased permeability to TH appeared in the CerNH24-containing samples annealed at 80 °C/H₂O relative to the same samples annealed at 90 °C. The flux of TH in the control 0/100 samples (90 °C) was 0.07 ± 0.03 $\mu\text{g}/\text{cm}^2/\text{h}$, which corresponded to previous results in similar samples ($0.09 \pm$

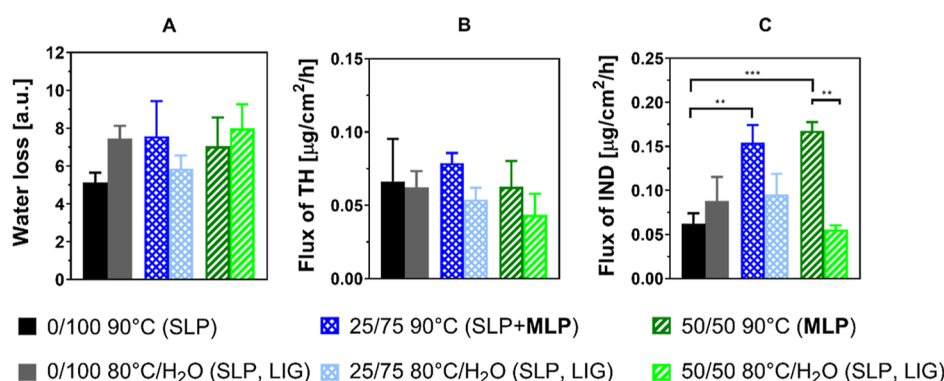


Figure 9. Permeability of the lipid films prepared at the CerNH24/CerNS24 molar ratios 0/100, 25/75, and 50/50 (LIG—separated lignoceric acid detected): water loss (panel A); the steady-state flux of theophylline (TH) (panel B); the steady-state flux of indomethacin (IND) (panel C); $n = 4–10$; n is the number of pertinent samples. Data are presented as the means \pm standard errors of the mean. Statistical significance compared to the control: ** $p < 0.01$; *** $p < 0.001$.

$0.02 \mu\text{g}/\text{cm}^2/\text{h}$ in ref 61). The lowest TH flux ($0.04 \pm 0.01 \mu\text{g}/\text{cm}^2/\text{h}$) was found in the 50/50 samples annealed at $80^\circ\text{C}/\text{H}_2\text{O}$.

Finally, the permeation experiment with IND as a model permeant revealed statistically significant differences among the studied samples. In the lipid films annealed at 90°C , the partial replacement of CerNS24 with CerNH24 in the 25/75 and 50/50 samples increased the IND flux to 0.15 ± 0.02 and $0.17 \pm 0.01 \mu\text{g}/\text{cm}^2/\text{h}$, respectively, relative to $0.06 \pm 0.01 \mu\text{g}/\text{cm}^2/\text{h}$ in the 0/100 sample.

In contrast, the IND flux through the samples annealed at $80^\circ\text{C}/\text{H}_2\text{O}$ did not significantly change among the 0/100, 25/75, and 50/50 samples (0.09 ± 0.02 , 0.10 ± 0.02 , and $0.06 \pm 0.01 \mu\text{g}/\text{cm}^2/\text{h}$, respectively). The samples with CerNH24 annealed at $80^\circ\text{C}/\text{H}_2\text{O}$ were apparently (the 25/75 samples; $p = 0.22$) or significantly less permeable to IND (the 50/50 samples; $p = 0.001$) than the same samples annealed at 90°C . These samples did not differ in the lipid composition but in the periodical structure, which was induced by modifications of the annealing method. The CerNH24-containing lipid films forming an MLP or an MLP and an SLP were significantly more permeable to IND than the same samples forming only SLP. The phase-separated LIG linked to the presence of interphase boundaries in the samples annealed at $80^\circ\text{C}/\text{H}_2\text{O}$ did not induce higher permeability.

DISCUSSION

The formation of MLP with $d = 10.6–10.8$ nm has been reported several times for simple Cer-based models based on CerNH24,⁴⁵ CerNS24,³⁹ bovine brain NS-type Cer ($d = 10.4$ nm),⁴⁰ and Cer analogue 3-deoxy-*N*-lignoceroyl sphingosine.⁴⁴ In this study, we have shown that lipid films of the same composition can form different structures when exposed to different conditions during their formation. The Cer chemical structure, sample preparation, and annealing method determine both the lamellar organization (SLP or MLP) and the lipid lamellar alignment relative to the supporting wafer. The structures are formed during the solidification of lipid melts in a thin film supported by a wafer. In this process, the system expresses considerable responsiveness to external conditions. The data showed that the structures formed are kinetically determined. Under the given conditions, the structures are kinetically favorable but most likely do not represent a thermodynamically stable structure (they do not have the lowest free energy).

The lipids used in our study serve as constituents of the skin permeability barrier. The repeat period of MLP did not change within the range of ± 0.02 nm when we compared the XRD measured at room humidity and the ND at 98% RH. The structure practically does not swell, and its repeat period exceeds twice the maximal length of the longest molecule within the composition, the Cer molecule in a fully extended conformation. The structural arrangement of the studied system does not allow it to accommodate a large amount of water.

The raw XRD pattern of MLP typically showed a higher intensity for even orders and a lower intensity for odd orders. This pattern was apparent despite the 1st order reflection not being recorded by the XRD, but it was detected with a neutron diffractometer. The relative intensity of the 1st order reflection was substantially lower compared to that of the 2nd order in the ND experiment. The low intensity of the 1st diffraction order appears to be a common characteristic of MLP diffraction patterns and the long lamellar phase observed in isolated human skin lipids or skin barrier models.^{23,28,29} Therefore, the architecture of these phases can share some principles, but there are also differences. The lamellar XRD reflections of the MLP alternate in their intensities. Generally, the patterns with alternating reflections of low and high intensity are typical for systems that include two apposed asymmetric bilayers, symmetric bilayers with asymmetrically distributed protein, or a combination of the two.^{28,66,67,92} White et al. suggested that alternating intensities arise whenever the membranes of the unit cell have a nearly symmetric electron density. If, however, the membranes of the unit cell are highly asymmetric, the alternating intensity pattern no longer prevails.²⁸ For example, the electron density profile of myelin contains a membrane pair of two plasma cell membranes, resulting in a repeating sequence of the broad/narrow bands of the high relative electron density separated by the bands of the low relative electron density.⁹³ Similar diffraction patterns were also reported in the L_γ phase of the pulmonary surfactant,⁶⁷ lipid–peptide complexes,⁶⁶ or mitochondrial lipids.⁹²

The alternating sequence of broad/narrow bands of low relative NSLD was also extracted from our diffractometric data. This was allowed when we reconstructed the relative NSLD profiles using all possible combinations of phase angles. After discarding the nonrealistic NSLD distributions, we obtained two very similar solutions containing two alternating domains

of low NSLD: bands of ~ 6 and ~ 4 nm width, respectively. The simplified molecular model (Figure 7) is based on the extended conformation of Cer molecules. The molecular model allows the intermolecular hydrogen bonding of the hydrophilic functional groups in the polar regions. The hydrogen bond network that forms a sheet of infinite bond systems in the center of the lipid layering was also described in the monocystal of *N*-lignoceroylphytosphingosine.¹¹

The water distribution profile was calculated as the difference between the relative NSLD at 100 and 8% D₂O content. In the evaluation according to Franks and Lieb⁵¹ (Figure 6B), the water distribution profile resulted in slightly negative values (between 0 and -10) in the hydrophobic regions. Similar results were obtained in the second method (Figure 7C). The reason for this effect is not clear. We speculate that it is caused by the limited number of F_h used to calculate the D₂O distribution profile. However, slightly negative values of the D₂O distribution were previously reported by Mojumdar et al.³⁸ and occurred in our further measurements (unpublished data). The problem needs further investigation.

The lipid organization based on the extended Cer conformation is in agreement with previous results from Fourier transform infrared spectroscopy,^{90,94} XRD,³⁹ and ²H solid-phase NMR.⁹¹ It was proposed as a basic structural unit of SC lipid sheets^{25,87} and developed as a model of the SC lipid matrix using molecular dynamics simulations.⁹⁵

The proposed molecular arrangement could serve as a basic motif of the ceramide-based water-resistant barrier. The extended conformation of Cer molecules and the preferential interaction of each Cer chain with different lipid species determine the asymmetry across the lamella. Further implications are that (i) the possibility of water uptake into such an arrangement is minimalized; (ii) each leaflet could attain a different lever of chain fluidity; (iii) stabilization of the arrangement by a system of intermolecular hydrogen bonds; and (iv) the laminated structure of the stacking is similar to the model proposed by Norlén and Pascher.⁹⁶

Next, we attempted to link the lipid arrangement with permeability. We are aware that XRD was measured at ambient room temperature and humidity and characterized the lipid film structures as they were before the permeation experiment. During the permeation, the lipid films are exposed to the water gradient between the donor and acceptor compartments, which is equilibrated at a physiological skin temperature of 32 °C. Such conditions cannot be reached in our XRD setup. However, even at 100% RH, the SC lipids bind only ~ 2 water molecules per lipid.³⁷ Although we cannot rule out changes in the lipid films caused by hydration and temperature, the permeability of our model lipid films to IND was found to be susceptible to their initial lamellar arrangement as detected by XRD.

Previously, 1.5-fold higher water loss and fourfold higher IND flux were observed due to the replacement of CerNS24 (with SLP) with CerNH24 (with MLP) in lipid models annealed at 90 °C.³⁷ However, it was not possible to distinguish whether those changes were caused by different Cer headgroups or different long-range arrangements of the lipids. In this study, the 50/50 model that formed an MLP was approximately threefold more permeable to IND than the sample with the same composition that formed an SLP. Thus, the MLP appears to be a less advantageous arrangement than

the SLP in terms of sample permeability, despite its longer repeat distance.

CONCLUSIONS

The preparation process and the sample treatment determine the structure and barrier properties of the lipid films. CerNH24-based lipid films can form an SLP or an MLP depending on the annealing conditions. The supposed molecular arrangement of the MLP correlated with a realistic NSLD profile selected from that reconstructed using all the possible phase angle combinations in two subsequent steps. The lipid films that formed an MLP were more permeable to IND than those with the same composition that formed an SLP. A simple lipid mixture can be modulated so that it creates films of different structures with different degrees of lipid alignment and barrier properties. As the lipids are susceptible to the conditions encountered during their assembly in the model, the question arises whether these lipids can also form different nanostructures when they are exposed to abnormal conditions in vivo.

ASSOCIATED CONTENT

Supporting Information

The Supporting Information is available free of charge at <https://pubs.acs.org/doi/10.1021/acsomega.2c04924>.

HPLC of model permeants; permeation data evaluation and statistics; XRD peak positions; 2D XRD patterns of the CerNH24/CerNS24/LIG/Chol samples; XRD pattern of the CerNH24/CerNS24/LIG/Chol/CholS sample; ND data evaluation; NSLD profiles of the CerNH24/CerNS24/LIG/Chol/CholS sample at 100% D₂O reconstructed from the first five F_h factors using all possible combinations of phase angles; and permeation profiles of the CerNH24/CerNS24/LIG/Chol samples (PDF)

AUTHOR INFORMATION

Corresponding Author

Petra Pullmannová – Skin Barrier Research Group, Charles University, Faculty of Pharmacy in Hradec Králové, 500 05 Hradec Králové, Czech Republic; orcid.org/0000-0001-5801-5094; Email: pullmanp@faf.cuni.cz

Authors

Barbora A. Čuřiková-Kindlová – Faculty of Chemical Technology, University of Chemistry and Technology Prague, 166 28 Prague, Czech Republic

Veronika Ondřejčková – Skin Barrier Research Group, Charles University, Faculty of Pharmacy in Hradec Králové, 500 05 Hradec Králové, Czech Republic

Andrej Kováčik – Skin Barrier Research Group, Charles University, Faculty of Pharmacy in Hradec Králové, 500 05 Hradec Králové, Czech Republic; orcid.org/0000-0002-5597-3155

Kristýna Dvořáková – Faculty of Chemical Technology, University of Chemistry and Technology Prague, 166 28 Prague, Czech Republic

Lucia Dulanská – Skin Barrier Research Group, Charles University, Faculty of Pharmacy in Hradec Králové, 500 05 Hradec Králové, Czech Republic

Robert Georgii – Heinz Maier-Leibnitz Zentrum (MLZ), Technische Universität München, 85748 Garching, Germany

Adam Majcher – Skin Barrier Research Group, Charles University, Faculty of Pharmacy in Hradec Králové, 500 05 Hradec Králové, Czech Republic

Jaroslav Maixner – Faculty of Chemical Technology, University of Chemistry and Technology Prague, 166 28 Prague, Czech Republic

Norbert Kučerka – Faculty of Pharmacy, Comenius University Bratislava, 832 32 Bratislava, Slovakia; Frank Laboratory of Neutron Physics, Joint Institute for Nuclear Research, 141980 Dubna, Russia; orcid.org/0000-0002-1075-6640

Jarmila Zbytovská – Skin Barrier Research Group, Charles University, Faculty of Pharmacy in Hradec Králové, 500 05 Hradec Králové, Czech Republic; Faculty of Chemical Technology, University of Chemistry and Technology Prague, 166 28 Prague, Czech Republic

Kateřina Vávrová – Skin Barrier Research Group, Charles University, Faculty of Pharmacy in Hradec Králové, 500 05 Hradec Králové, Czech Republic

Complete contact information is available at:

<https://pubs.acs.org/10.1021/acsomega.2c04924>

Author Contributions

P.P. prepared samples for XRD and ND, analyzed data, and wrote the manuscript; BAČ-K, V.O., K.D., and R.G. performed ND, A.K. and L.D. performed permeation experiments, A.M. and A.K. synthesized CerNH₂₄, J.M. and J.Z. performed XRD, N.K. calculated continuous Fourier transforms, and K.V. designed the research.

Notes

The authors declare no competing financial interest.

ACKNOWLEDGMENTS

The study was supported by the Czech Science Foundation (22-20839K and 19-09600S), Charles University (SVV 260 547), and by the project EFSA-CDN (no. CZ.02.1.01/0.0/0.0/16_019/0000841) co-funded by ERDF. The neutron measurements were performed at MIRA, Heinz Maier-Leibnitz Zentrum (MLZ) under the proposal #14603.

ABBREVIATIONS

Cer, ceramide(s); CerNH₂₄, *N*-lignoceroyl *D*-erythro-6-hydroxysphingosine; CerNS₂₄, *N*-lignoceroyl *D*-erythro-sphingosine; Chol, cholesterol; CholS, sodium cholesteryl sulfate; FFA, free fatty acid(s); FFA(16:0–24:0), mixture of free fatty acids with 16, 18, 20, 22 and 24 carbons; IND, indomethacin; LIG, lignoceric acid; MLP, medium lamellar phase; ND, neutron diffraction; NSLD, neutron scattering length density; PBS, phosphate-buffered saline; RH, relative humidity; SC, stratum corneum; SLP, short lamellar phase; TH, theophylline; XRD, X-ray diffraction

REFERENCES

- (1) Koch, K.; Barthlott, W. Plant Epicuticular Waxes: Chemistry, Form, Self-Assembly and Function. *Nat. Prod. Commun.* **2006**, *1*, 1934578X0600101123.
- (2) McCulley, J. P.; Shine, W. E. The Lipid Layer: The Outer Surface of the Ocular Surface Tear Film. *Biosci. Rep.* **2001**, *21*, 407–418.
- (3) Chen, J.; Nichols, K. K. Comprehensive shotgun lipidomics of human meibomian gland secretions using MS/MSall with successive switching between acquisition polarity modes. *J. Lipid Res.* **2018**, *59*, 2223–2236.

- (4) Ginzel, M. D.; Blomquist, G. J. Insect Hydrocarbons: Biochemistry and Chemical Ecology. In *Extracellular Composite Matrices in Arthropods*; Cohen, E., Moussian, B., Eds.; Springer International Publishing: Cham, 2016; pp 221–252.

- (5) Méndez, S.; Martí, M.; Barba, C.; Parra, J. L.; Coderch, L. Thermotropic Behavior of Ceramides and Their Isolation from Wool. *Langmuir* **2007**, *23*, 1359–1364.

- (6) Cwiklik, L. Tear film lipid layer: A molecular level view. *Biochim. Biophys. Acta* **2016**, *1858*, 2421–2430.

- (7) Elias, P. M. Epidermal Lipids, Membranes, and Keratinization. *Int. J. Dermatol.* **1981**, *20*, 1–19.

- (8) Wertz, P. W. Stratum corneum lipids and water. *Exog. Dermatol.* **2004**, *3*, 53–56.

- (9) Kováčik, A.; Opálka, L.; Šilarová, M.; Roh, J.; Vávrová, K. Synthesis of 6-hydroxyceramide using ruthenium-catalyzed hydro-silylation–protodesilylation. Unexpected formation of a long periodicity lamellar phase in skin lipid membranes. *RSC Adv.* **2016**, *6*, 73343–73350.

- (10) Opálka, L.; Kováčik, A.; Sochorová, M.; Roh, J.; Kuneš, J.; Lenčo, J.; Vávrová, K. Scalable Synthesis of Human Ultralong Chain Ceramides. *Org. Lett.* **2015**, *17*, 5456–5459.

- (11) Dahlén, B.; Pascher, I. Molecular arrangements in sphingolipids. Thermotropic phase behaviour of tetracosanoylphosphatidylcholine. *Chem. Phys. Lipids* **1979**, *24*, 119–133.

- (12) Futerman, A. H.; Hannun, Y. A. The complex life of simple sphingolipids. *EMBO Rep.* **2004**, *5*, 777–782.

- (13) Merrill, A. H. De Novo Sphingolipid Biosynthesis: A Necessary, but Dangerous, Pathway. *J. Biol. Chem.* **2002**, *277*, 25843–25846.

- (14) Sandhoff, R. Very long chain sphingolipids: Tissue expression, function and synthesis. *FEBS Lett.* **2010**, *584*, 1907–1913.

- (15) Hannun, Y. A. Functions of Ceramide in Coordinating Cellular Responses to Stress. *Science* **1996**, *274*, 1855–1859.

- (16) Hannun, Y. A.; Obeid, L. M. Principles of bioactive lipid signalling: lessons from sphingolipids. *Nat. Rev. Mol. Cell Biol.* **2008**, *9*, 139–150.

- (17) Burgert, A.; Schlegel, J.; Bécam, J.; Doose, P. S.; Bieberich, E.; Schubert-Unkmeier, A.; Sauer, M. Characterization of plasma membrane ceramides by super-resolution microscopy. *Angew. Chem., Int. Ed. Engl.* **2017**, *56*, 6131–6135.

- (18) Kraft, M. L. Sphingolipid Organization in the Plasma Membrane and the Mechanisms That Influence It. *Front. Cell Dev. Biol.* **2017**, *4*, 154.

- (19) Landmann, L. The epidermal permeability barrier. Comparison between in vivo and in vitro lipid structures. *Eur. J. Cell Biol.* **1984**, *33*, 258–64.

- (20) de Jager, M.; Groenink, W.; van der Spek, J.; Janmaat, C.; Gooris, G.; Ponc, M.; Bouwstra, J. Preparation and characterization of a stratum corneum substitute for in vitro percutaneous penetration studies. *Biochim. Biophys. Acta* **2006**, *1758*, 636–644.

- (21) Goldsmith, L. A.; Baden, H. P. Uniquely Oriented Epidermal Lipid. *Nature* **1970**, *225*, 1052–1053.

- (22) Bouwstra, J. A.; Gooris, G. S.; Cheng, K.; Weerheim, A.; Bras, W.; Ponc, M. Phase behavior of isolated skin lipids. *J. Lipid Res.* **1996**, *37*, 999–1011.

- (23) Bouwstra, J. A.; Gooris, G. S.; van der Spek, J. A.; Bras, W. Structural Investigations of Human Stratum Corneum by Small-Angle X-Ray Scattering. *J. Invest. Dermatol.* **1991**, *97*, 1005–1012.

- (24) McIntosh, T. J.; Stewart, M. E.; Downing, D. T. X-ray Diffraction Analysis of Isolated Skin Lipids: Reconstitution of Intercellular Lipid Domains. *Biochemistry* **1996**, *35*, 3649–3653.

- (25) Iwai, I.; Han, H.; Hollander, L. d.; Svensson, S.; Öfverstedt, L.-G.; Anwar, J.; Brewer, J.; Bloksgaard, M.; Laloeuf, A.; Nosek, D.; Masich, S.; Bagatolli, L. A.; Skoglund, U.; Norlén, L. The Human Skin Barrier Is Organized as Stacked Bilayers of Fully Extended Ceramides with Cholesterol Molecules Associated with the Ceramide Sphingoid Moiety. *J. Invest. Dermatol.* **2012**, *132*, 2215–2225.

- (26) Mojumdar, E. H.; Gooris, G. S.; Groen, D.; Barlow, D. J.; Lawrence, M. J.; Demé, B.; Bouwstra, J. A. Stratum corneum lipid matrix: Location of acyl ceramide and cholesterol in the unit cell of

- the long periodicity phase. *Biochim. Biophys. Acta* **2016**, *1858*, 1926–1934.
- (27) Swartzendruber, D. C.; Wertz, P. W.; Kitko, D. J.; Madison, K. C.; Downing, D. T. Molecular models of the Intercellular Lipid Lamellae in Mammalian Stratum Corneum. *J. Invest. Dermatol.* **1989**, *92*, 251–257.
- (28) White, S. H.; Mirejovsky, D.; King, G. I. Structure of lamellar lipid domains and corneocyte envelopes of murine stratum corneum. An x-ray diffraction study. *Biochemistry* **1988**, *27*, 3725–3732.
- (29) Hou, S. Y. E.; Mitra, A. K.; White, S. H.; Menon, G. K.; Ghadially, R.; Elias, P. M. Membrane Structures in Normal and Essential Fatty Acid-Deficient Stratum Corneum: Characterization by Ruthenium Tetroxide Staining and X-Ray Diffraction. *J. Invest. Dermatol.* **1991**, *96*, 215–223.
- (30) Bouwstra, J. A.; Gooris, G. S.; Vries, M. A. S.; van der Spek, J. A.; Bras, W. Structure of human stratum corneum as a function of temperature and hydration: A wide-angle X-ray diffraction study. *Int. J. Pharm.* **1992**, *84*, 205–216.
- (31) Garson, J. C.; Doucet, J.; L  v  que, J. L.; Tsoucaris, G. Oriented structure in human stratum corneum revealed by X-ray diffraction. *J. Invest. Dermatol.* **1991**, *96*, 43–49.
- (32) Bouwstra, J. A.; Gooris, G. S.; Dubbelaar, F. E. R.; Weerheim, A. M.; IJzerman, A. P.; Ponc, M. Role of ceramide 1 in the molecular organization of the stratum corneum lipids. *J. Lipid Res.* **1998**, *39*, 186–196.
- (33) Schreiner, V.; Pfeiffer, G. S.; Lanzend  rfer, S.; Wenck, G.; Diembeck, H.; Gooris, W.; Proksch, E.; Bouwstra, J. Barrier Characteristics of Different Human Skin Types Investigated with X-Ray Diffraction, Lipid Analysis, and Electron Microscopy Imaging. *J. Invest. Dermatol.* **2000**, *114*, 654–660.
- (34) Janssens, M.; van Smeden, J.; Gooris, G. S.; Bras, W.; Portale, G.; Caspers, P. J.; Vreeken, R. J.; Kezic, S.; Lavrijzen, A. P. M.; Bouwstra, J. A. Lamellar Lipid Organization and Ceramide Composition in the Stratum Corneum of Patients with Atopic Eczema. *J. Invest. Dermatol.* **2011**, *131*, 2136–2138.
- (35) Kiselev, M. A.; Ryabova, N. Y.; Balagurov, A. M.; Dante, S.; Hauss, T.; Zbytovska, J.; Wartewig, S.; Neubert, R. H. H. New insights into the structure and hydration of a stratum corneum lipid model membrane by neutron diffraction. *Eur. Biophys. J.* **2005**, *34*, 1030–1040.
- (36) Schr  ter, A.; Kessner, D.; Kiselev, M. A.; Hau  , T.; Dante, S.; Neubert, R. H. H. Basic Nanostructure of Stratum Corneum Lipid Matrices Based on Ceramides [EOS] and [AP]: A Neutron Diffraction Study. *Biophys. J.* **2009**, *97*, 1104–1114.
- (37) Groen, D.; Gooris, G. S.; Barlow, D. J.; Lawrence, M. J.; van Mechelen, J. B.; Dem  , B.; Bouwstra, J. A. Disposition of Ceramide in Model Lipid Membranes Determined by Neutron Diffraction. *Biophys. J.* **2011**, *100*, 1481–1489.
- (38) Mojumdar, E. H.; Gooris, G. S.; Barlow, D. J.; Lawrence, M. J.; Deme, B.; Bouwstra, J. A. Skin lipids: localization of ceramide and fatty acid in the unit cell of the long periodicity phase. *Biophys. J.* **2015**, *108*, 2670–2679.
- (39) Pullmannov  , P.; Ermakova, E.; Kov  cik, A.; Op  lka, L.; Maixner, J.; Zbytovsk  , J.; Ku  cerka, N.; V  vrov  , K. Long and very long lamellar phases in model stratum corneum lipid membranes. *J. Lipid Res.* **2019**, *60*, 963–971.
- (40) Parrott, D. T.; Turner, J. E. Mesophase formation by ceramides and cholesterol: a model for stratum corneum lipid packing? *Biochim. Biophys. Acta* **1993**, *1147*, 273–276.
- (41) de Jager, M. W.; Gooris, G. S.; Dolbnya, I. P.; Bras, W.; Ponc, M.; Bouwstra, J. A. The phase behaviour of skin lipid mixtures based on synthetic ceramides. *Chem. Phys. Lipids* **2003**, *124*, 123–134.
- (42) Bouwstra, J. A.; Honeywell-Nguyen, P. L.; Gooris, G. S.; Ponc, M. Structure of the skin barrier and its modulation by vesicular formulations. *Prog. Lipid Res.* **2003**, *42*, 1–36.
- (43) Kov  cik, A.; Vogel, A.; Adler, J.; Pullmannov  , P.; V  vrov  , K.; Huster, D. Probing the role of ceramide hydroxylation in skin barrier lipid models by 2H solid-state NMR spectroscopy and X-ray powder diffraction. *Biochim. Biophys. Acta, Biomembr.* **2018**, *1860*, 1162–1170.
- (44) Kov  cik, A.; Pullmannov  , P.; Pavl  kov  , L.; Maixner, J.; V  vrov  , K. Behavior of 1-Deoxy-, 3-Deoxy- and N-Methyl-Ceramides in Skin Barrier Lipid Models. *Sci. Rep.* **2020**, *10*, 1–12.
- (45) Kov  cik, A.; S  larov  , M.; Pullmannov  , P.; Maixner, J.; V  vrov  , K. Effects of 6-Hydroxyceramides on the Thermotropic Phase Behavior and Permeability of Model Skin Lipid Membranes. *Langmuir* **2017**, *33*, 2890–2899.
- (46)   kolov  , B.; Janu  sov  , B.; Zbytovsk  , J.; Gooris, G.; Bouwstra, J.; Slep  cka, P.; Berka, P.; Roh, J.; Pal  t, K.; Hrab  lek, A.; V  vrov  , K. Ceramides in the Skin Lipid Membranes: Length Matters. *Langmuir* **2013**, *29*, 15624–15633.
- (47) Georgii, R.; Weber, T.; Brandl, G.; Skoulatos, M.; Janoschek, M.; M  hlbauer, S.; Pfeleiderer, C.; B  ni, P. The multi-purpose three-axis spectrometer (TAS) MIRA at FRM II. *Nucl. Instrum. Methods Phys. Res., Sect. A* **2018**, *881*, 60–64.
- (48) Ku  cerka, N.; Nieh, M.-P.; Pencer, J.; Sachs, J. N.; Katsaras, J. What determines the thickness of a biological membrane. *Gen. Physiol. Biophys.* **2009**, *28*, 117–125.
- (49) Tristram-Nagle, S.; Liu, Y.; Legleiter, J.; Nagle, J. F. Structure of Gel Phase DMPC Determined by X-Ray Diffraction. *Biophys. J.* **2002**, *83*, 3324–3335.
- (50) Nagle, J. F.; Akabori, K.; Treece, B. W.; Tristram-Nagle, S. Determination of mosaicity in oriented stacks of lipid bilayers. *Soft Matter* **2016**, *12*, 1884–1891.
- (51) Franks, N. P.; Lieb, W. R. The structure of lipid bilayers and the effects of general anaesthetics: An X-ray and neutron diffraction study. *J. Mol. Biol.* **1979**, *133*, 469–500.
- (52) Ryabova, N. Y.; Kiselev, M. A.; Dante, S.; Hau  , T.; Balagurov, A. M. Investigation of stratum corneum lipid model membranes with free fatty acid composition by neutron diffraction. *Eur. Biophys. J.* **2010**, *39*, 1167–1176.
- (53) Dante, S.; Hauss, T.; Dencher, N. A. β -Amyloid 25 to 35 Is Intercalated in Anionic and Zwitterionic Lipid Membranes to Different Extents. *Biophys. J.* **2002**, *83*, 2610–2616.
- (54) Schmitt, T.; Lange, S.; Sonnenberger, S.; Dobner, B.; Dem  , B.; Langner, A.; Neubert, R. H. H. The long periodicity phase (LPP) controversy part I: The influence of a natural-like ratio of the CER[EOS] analogue [EOS]-br in a CER[NP]/[AP] based stratum corneum modelling system: A neutron diffraction study. *Biochim. Biophys. Acta* **2019**, *1861*, 306–315.
- (55) Hrubov  k, P.; Kondela, T.; Ermakova, E.; Ku  cerka, N. Application of small-angle neutron diffraction to the localization of general anesthetics in model membranes. *Eur. Biophys. J.* **2019**, *48*, 447–455.
- (56) Ku  cerka, N.; Hrubov  k, P.; Dushanov, E.; Kondela, T.; Kholmurodov, K. T.; Gallov  , J.; Balgav  , P. Location of the general anesthetic n-decane in model membranes. *J. Mol. Liq.* **2019**, *276*, 624–629.
- (57) Samoylova, N. Y.; Kiselev, M. A.; Hau  , T. Effect of DMSO, urea and ethanol on hydration of stratum corneum model membrane based on short-chain length ceramide [AP]. *Chem. Phys. Lipids* **2019**, *221*, 1–7.
- (58) Kirschner, D. A.; Sidman, R. L. X-ray diffraction study of myelin structure in immature and mutant mice. *Biochim. Biophys. Acta* **1976**, *448*, 73–87.
- (59) Ku  cerka, N.; Pencer, J.; Sachs, J. N.; Nagle, J. F.; Katsaras, J. Curvature Effect on the Structure of Phospholipid Bilayers. *Langmuir* **2007**, *23*, 1292.
- (60) Pullmannov  , P.; Sta  nkov  , K.; Posp  silov  , M.;   kolov  , B.; Zbytovsk  , J.; V  vrov  , K. Effects of sphingomyelin/ceramide ratio on the permeability and microstructure of model stratum corneum lipid membranes. *Biochim. Biophys. Acta* **2014**, *1838*, 2115–2126.
- (61) Pullmannov  , P.; Pavl  kov  , L.; Kov  cik, A.; Sochorov  , M.;   kolov  , B.; Slep  cka, P.; Maixner, J.; Zbytovsk  , J.; V  vrov  , K. Permeability and microstructure of model stratum corneum lipid membranes containing ceramides with long (C16) and very long (C24) acyl chains. *Biophys. Chem.* **2017**, *224*, 20–31.

- (62) Schmitt, T.; Gupta, R.; Lange, S.; Sonnenberger, S.; Dobner, B.; Hauß, T.; Rai, B.; Neubert, R. H. H. Impact of the ceramide subspecies on the nanostructure of stratum corneum lipids using neutron scattering and molecular dynamics simulations. Part I: impact of CER[NS]. *Chem. Phys. Lipids* **2018**, *214*, 58–68.
- (63) McIntosh, T. J.; Waldbillig, R. C.; Robertson, J. D. The molecular organization of asymmetric lipid bilayers and lipid-peptide complexes. *Biochim. Biophys. Acta* **1977**, *466*, 209–230.
- (64) Worthington, C. R.; Blaurock, A. E. A Structural Analysis of Nerve Myelin. *Biophys. J.* **1969**, *9*, 970–990.
- (65) Ranck, J. L.; Zaccai, G.; Luzzati, V. The structure of a lipid-water lamellar phase containing two types of lipid monolayers. An X-ray and neutron scattering study. *J. Appl. Crystallogr.* **1980**, *13*, 505–512.
- (66) Silva, T.; Claro, B.; Silva, B. F. B.; Vale, N.; Gomes, P.; Gomes, M. S.; Funari, S. S.; Teixeira, J.; Uhríková, D.; Bastos, M. Unravelling a Mechanism of Action for a Cecropin A-Melittin Hybrid Antimicrobial Peptide: The Induced Formation of Multilamellar Lipid Stacks. *Langmuir* **2018**, *34*, 2158–2170.
- (67) Kumar, K.; Chavarha, M.; Loney, R. W.; Weiss, T. M.; Rananavare, S. B.; Hall, S. B. The L γ Phase of Pulmonary Surfactant. *Langmuir* **2018**, *34*, 6601–6611.
- (68) Abrahamsson, S.; von Sydow, E. Variation of unit-cell dimensions of a crystal form of long normal chain carboxylic acids. *Acta Crystallogr.* **1954**, *7*, 591–592.
- (69) Marsh, D. Lateral order in gel, subgel and crystalline phases of lipid membranes: Wide-angle X-ray scattering. *Chem. Phys. Lipids* **2012**, *165*, 59–76.
- (70) Pascher, I.; Sundell, S. Molecular arrangements in sphingolipids: crystal structure of the ceramide N-(2d,3d-dihydroxyoctadecanoyl)-phytosphingosine. *Chem. Phys. Lipids* **1992**, *62*, 79–86.
- (71) Dahlén, B.; Pascher, I. Molecular arrangements in sphingolipids. Crystal structure of N-tetracosanoylphytosphingosine. *Acta Crystallogr., Sect. B: Struct. Crystallogr. Cryst. Chem.* **1972**, *28*, 2396–2404.
- (72) Finegold, L. X. *Cholesterol in Membrane Models*; Taylor & Francis, 1992.
- (73) Katsaras, J.; Raghunathan, V. A.; Dufourc, E. J.; Dufourcq, J. Evidence for a Two-Dimensional Molecular Lattice in Subgel Phase DPPC Bilayers. *Biochemistry* **1995**, *34*, 4684–4688.
- (74) McIntosh, T. J. The effect of cholesterol on the structure of phosphatidylcholine bilayers. *Biochim. Biophys. Acta* **1978**, *513*, 43–58.
- (75) McIntosh, T. J.; Waldbillig, R. C.; Robertson, J. D. Lipid bilayer ultrastructure: Electron density profiles and chain tilt angles as determined by X-ray diffraction. *Biochim. Biophys. Acta* **1976**, *448*, 15–33.
- (76) Khare, R. S.; Worthington, C. R. The structure of oriented sphingomyelin bilayers. *Biochim. Biophys. Acta* **1978**, *514*, 239–254.
- (77) Khare, R. S.; Worthington, C. R. An X-Ray Diffraction Study of Sphingomyelin-Cholesterol Interaction in Oriented Bilayers. *Mol. Cryst. Liq. Cryst.* **1977**, *38*, 195–206.
- (78) Ensikat, H. J.; Boese, M.; Mader, W.; Barthlott, W.; Koch, K. Crystallinity of plant epicuticular waxes: electron and X-ray diffraction studies. *Chem. Phys. Lipids* **2006**, *144*, 45–59.
- (79) Bouwstra, J. A.; Thewalt, J.; Gooris, G. S.; Kitson, N. A Model Membrane Approach to the Epidermal Permeability Barrier: An X-ray Diffraction Study. *Biochemistry* **1997**, *36*, 7717–7725.
- (80) Worcester, D. L.; Franks, N. P. Structural analysis of hydrated egg lecithin and cholesterol bilayers II. Neutron diffraction. *J. Mol. Biol.* **1976**, *100*, 359–378.
- (81) Ruettinger, A.; Kiselev, M. A.; Hauss, T.; Dante, S.; Balagurov, A. M.; Neubert, R. H. H. Fatty acid interdigitation in stratum corneum model membranes: a neutron diffraction study. *Eur. Biophys. J.* **2008**, *37*, 759–771.
- (82) Rerek, M. E.; Markovic, B.; Van Wyck, D.; Garidel, P.; Mendelsohn, R.; Moore, D. J. Phytosphingosine and Sphingosine Ceramide Headgroup Hydrogen Bonding: Structural Insights through Thermotropic Hydrogen/Deuterium Exchange. *J. Phys. Chem. B* **2001**, *105*, 9355–9362.
- (83) Garidel, P. Structural organisation and phase behaviour of a stratum corneum lipid analogue: ceramide 3A. *Phys. Chem. Chem. Phys.* **2006**, *8*, 2265.
- (84) Garidel, P.; Fölting, B.; Schaller, I.; Kerth, A. The microstructure of the stratum corneum lipid barrier: Mid-infrared spectroscopic studies of hydrated ceramide:palmitic acid:cholesterol model systems. *Biophys. Chem.* **2010**, *150*, 144–56.
- (85) Banc, A.; Charbonneau, C.; Dahesh, M.; Appavou, M.-S.; Fu, Z.; Morel, M.-H.; Ramos, L. Small angle neutron scattering contrast variation reveals heterogeneities of interactions in protein gels. *Soft Matter* **2016**, *12*, 5340–5352.
- (86) Hill, J. R.; Wertz, P. W. Molecular models of the intercellular lipid lamellae from epidermal stratum corneum. *Biochim. Biophys. Acta* **2003**, *1616*, 121–126.
- (87) Narangifard, A.; Wennberg, C. L.; den Hollander, L.; Iwai, I.; Han, H.; Lundborg, M.; Masich, S.; Lindahl, E.; Daneholt, B.; Norlén, L. Molecular Reorganization during the Formation of the Human Skin Barrier Studied In Situ. *J. Invest. Dermatol.* **2021**, *141*, 1243–1253.
- (88) Narangifard, A.; den Hollander, L.; Wennberg, C. L.; Lundborg, M.; Lindahl, E.; Iwai, I.; Han, H.; Masich, S.; Daneholt, B.; Norlén, L. Human skin barrier formation takes place via a cubic to lamellar lipid phase transition as analyzed by cryo-electron microscopy and EM-simulation. *Exp. Cell Res.* **2018**, *366*, 139–151.
- (89) Lundborg, M.; Narangifard, A.; Wennberg, C. L.; Lindahl, E.; Daneholt, B.; Norlén, L. Human skin barrier structure and function analyzed by cryo-EM and molecular dynamics simulation. *J. Struct. Biol.* **2018**, *203*, 149–161.
- (90) Školová, B.; Hudská, K.; Pullmannová, P.; Kováčik, A.; Palát, K.; Roh, J.; Fleddermann, J.; Estrela-Lopis, I.; Vávrová, K. Different Phase Behavior and Packing of Ceramides with Long (C16) and Very Long (C24) Acyls in Model Membranes: Infrared Spectroscopy Using Deuterated Lipids. *J. Phys. Chem. B* **2014**, *118*, 10460–10470.
- (91) Engberg, O.; Kováčik, A.; Pullmannová, P.; Juhaščík, M.; Opálka, L.; Huster, D.; Vávrová, K. The Sphingosine and Acyl Chains of Ceramide [NS] Show Very Different Structure and Dynamics That Challenge Our Understanding of the Skin Barrier. *Angew. Chem., Int. Ed.* **2020**, *59*, 17383–17387.
- (92) Ranck, J. L.; Zaccai, G.; Luzzati, V. The structure of a lipid-water lamellar phase containing two types of lipid monolayers. An X-ray and neutron scattering study. *J. Appl. Crystallogr.* **1980**, *13*, 505–512.
- (93) Avila, R. L.; Inouye, H.; Baek, R. C.; Yin, X.; Trapp, B. D.; Feltri, M. L.; Wrabetz, L.; Kirschner, D. A. Structure and stability of internodal myelin in mouse models of hereditary neuropathy. *J. Neuropathol. Exp. Neurol.* **2005**, *64*, 976–990.
- (94) Beddoes, C. M.; Gooris, G. S.; Bouwstra, J. A. Preferential arrangement of lipids in the long-periodicity phase of a stratum corneum matrix model. *J. Lipid Res.* **2018**, *59*, 2329–2338.
- (95) Antunes, E.; Cavaco-Paulo, A. Stratum corneum lipid matrix with unusual packing: A molecular dynamics study. *Colloids Surf., B* **2020**, *190*, 110928.
- (96) Norlén, L. Molecular skin barrier models and some central problems for the understanding of skin barrier structure and function. *Skin Pharmacol. Appl. Skin Physiol.* **2003**, *16*, 203–211.